AIAA SciTech Forum
8-12 January 2024, Orlando, FL
AIAA SCITECH 2024 Forum

10.2514/6.2024-1909

Aerodynamic Optimization of a Flying V Aircraft Based on the Reynolds-Averaged Navier-Stokes Equations

Rasam R.S. Yazdi*, Thomas A. Reist†, and David W. Zingg‡
Institute for Aerospace Studies, University of Toronto, 4925 Dufferin St, Toronto, Ontario, M3H 5T6, Canada

High-fidelity aerodynamic optimization based on the Reynolds-averaged Navier-Stokes equations is used to investigate the aerodynamic performance of the Flying V aircraft configuration. The Flying V aircraft's performance is assessed in the wide-body and single-aisle classes, sized to match the capabilities of the Airbus A350-900 and A320neo, respectively. The initial aircraft geometry is chosen to match the planform in Faggiano, F., Vos, R., Baan, M., and Dijk, R., AIAA Paper 2017-3589, and a cabin constraint models the required number of passengers, cargo pallets, and overall shape. Lift-constrained drag minimization is performed with freedom in section shape and twist, while the planform is also allowed to vary, particularly at the single-aisle size. Optimizations are also performed at various center-of-gravity positions to evaluate performance sensitivity to static margin at the wide-body size, while sensitivity to cruise altitude is investigated for the single-aisle Flying V aircraft. At a static margin of 6%, exclusive of nacelles, pylons, and excrescences, the optimized fixed-planform wide-body Flying V aircraft produces a cruise lift-to-drag ratio of about 25.5, while planform optimization enables a cruise lift-to-drag ratio of 27, both at an altitude of 13,000 m. The optimized single-aisle Flying V aircraft produces a cruise lift-to-drag ratio of 23.2 at an altitude of 13,711 m.

I. Nomenclature

A	=	Projected area of the aircraft
c	=	Chord at a given span station
C_p	=	Pressure coefficient
C_D	=	Total drag coefficient of the aircraft
C_L	=	Total lift coefficient of the aircraft
C_L/C_D	=	Lift-to-drag ratio of the aircraft
CG	=	Center of gravity as measured from the aircraft nose, normalized by mean aerodynamic chord
D	=	Total drag of the aircraft
K_n	=	Static margin
L	=	Reference length of the aircraft
N	=	Number of grid nodes
NP	=	Neutral point as measured from the aircraft nose, normalized by mean aerodynamic chord
x/c	=	X-position as measured from the aircraft nose, normalized by local chord
y/b	=	Y-position as measured from the aircraft centerline, normalized by span

II. Introduction

Ever since the introduction of the de Havilland Comet in 1952, conventional tube-and-wing (CTW) aircraft with a cylindrical fuselage and rear empennage have dominated commercial aviation. While significant improvements made in disciplines such as aerodynamics, structures, and propulsion have produced a substantial increase in efficiency, the basic configuration has remained virtually unchanged [1, 2]. In recent times, the truss-braced wing (TBW) and blended wing-body (BWB) configurations have garnered a lot of attention in academia and industry. In January 2023, NASA awarded Boeing a contract worth $450 million to build and test a full-sized transonic TBW demonstrator with an intent

*BASc Candidate, Division of Engineering Science, University of Toronto, rassam.yazdi@mail.utoronto.ca
†Research Associate, tom.reist@utoronto.ca.
‡University of Toronto Distinguished Professor in Computational Aerodynamics and Sustainable Aviation, david.zingg@utoronto.ca

to reduce fuel burn by 30% [3]. On a similar note, California start-up JetZero is preparing to fly a NASA-supported 1/8th-scale BWB demonstrator later this year, with the goal of having their aircraft in the hands of customers by 2030 [4]. Another promising configuration is the flying wing concept, which aims to integrate lift, trimming, and payload carriage into a single component [5].

Flying wings have been studied since before the Second World War, yet they are still rarely used in practical applications. The Northrop B-2 bomber is a pure flying wing not only to reduce its radar cross section, but also due to the substantial aerodynamic efficiency offered by this configuration [6]. Hesitance in commercial pursuit of this configuration can be attributed to uncertainty surrounding its stability and control properties, non-cylindrical pressure vessels for the cabin, emergency evacuation, and passenger acceptance [7]. Despite the aforementioned points, the large potential for wetted area and weight reduction makes the flying wing a candidate configuration for large gains in efficiency [1]. Flying wings can also be quieter that equivalent CTW's since the configuration lends itself well to top-mounted engines, allowing for the body to shield the ground from noise. A flying wing concept that has gained popularity recently is known as the Flying V due to its distinct V-shaped planform. While initially conceived and studied by Benad [8], TU Delft has continued to develop the concept in a variety of disciplines such as aerodynamics, structures, control, field performance, interior design, and airport operations [9]. In terms of aerodynamics, Faggiano et al. optimized the Flying V with respect to cruise performance [7] using an Euler equation solver paired with an empirical method to calculate viscous drag. They performed optimizations with freedom in aircraft planform and section shape at 5 wing stations to achieve a lift-to-drag ratio of 23.7. Subsequently, Oosterom et al. investigated the performance of a wide-body family of Flying V aircraft [10], performing simultaneous multidisciplinary design optimization for a three-aircraft family modelled after the A350-800, A350-900, and A350-1000 variants. This study used the same flow solution method employed by Faggiano et al.

Aerodynamic shape optimization based on the Reynolds-averaged Navier-Stokes (RANS) equations has been successfully applied to both BWB and TBW aircraft [11–15]. However, there have been limited RANS-based investigations performed on the Flying V configuration. A TU Delft paper by Van Luijk et al. performed RANS-based optimizations, but the scope was localized to the aircraft's outerwing [16]. This study will focus on applying high-fidelity aerodynamic optimization based on the RANS equations to the Flying V aircraft configuration to provide an assessment of its fuel efficiency potential in the wide-body and single-aisle classes. The objectives of this work are 1) to corroborate results obtained by Faggiano et al. [7], 2) to demonstrate that wave drag can be sufficiently reduced based on RANS analysis, 3) to investigate the scalability of the concept by assessing a single-aisle class Flying V aircraft, and 4) to expand the design space through planform freedom. Following Faggiano et al., the Flying V will be sized to match the payload and range of the Airbus A350-900 and A320neo for the wide-body and single-aisle variants, respectively, and optimizations are performed at the start-of-cruise condition [7]. Low-speed performance, field performance, and maximum lift coefficient are left out of the scope of this paper. Optimizations begin with design freedom in only section shape and twist for the wide-body aircraft, given the multidisciplinary implications of making changes to the planform. Subsequently, the planform is given freedom to vary in span, chord, and sweep, in search of the aerodynamically optimal aircraft shape and cabin layout for both classes of the Flying V aircraft.

A. Aerodynamic Shape Optimization Framework

The aerodynamic shape optimization framework used in this study can be broken down into three parts. Flow evaluation is accomplished using a multiblock Newton-Krylov-Schur solver paired with the Spalart-Allmaras turbulence model [17]. The solver is a parallel implicit method, making use of summation-by-parts operators for spatial discretization and simultaneous approximation terms for imposing boundary and block interface conditions. Second, geometry control is achieved through the free-form and axial deformation method, where free-form deformation (FFD) volumes provide local shape control, and global shape control is performed via axial curves that drive the FFD volumes. Following Gagnon and Zingg [18], the B-spline control points that define the aerodynamic surface are embedded within the FFD volumes, ensuring that the analytical definition of the surface is maintained. The third and final component is SNOPT [19], which is a gradient-based optimizer. The discrete adjoint method is used to evaluate objective and constraint gradients [20]. This framework has been extensively applied to the investigation of unconventional aircraft [13–15, 21], with a separate cross-validation study being carried out by Reist et al [22].

Table 1 General information regarding the full aircraft planform.

Planform Area [m^2]	Full Span [m]	Root Chord [m]	Tip Chord [m]
883.3	65.0	24.0	3.2

Table 2 Sectional breakdown of aircraft planform.

Sections	Leading Edge Sweep [°]	Quarter-Chord Sweep [°]	Taper Ratio [-]	Aspect Ratio [-]
I-II	64.40	63.50	0.833	1.12
II-III	64.40	59.21	0.354	1.17
III-IV	37.80	34.85	0.455	4.71

III. Initial Design Work

A. Development of Baseline Wide-Body Geometry

The baseline geometry in this project is modelled after the optimized aircraft developed by Faggiano et al. [7], which matches the top level requirements of the Airbus A350-900, a modern, state-of-the-art wide-body commercial aircraft. In terms of flight conditions, a cruise Mach number of 0.85 at an altitude of 13,000 m is assumed [7]. Geometric information is obtained through design tables and diagrams available in Faggiano et al. and TU Delft's Flying V website [23]. With that information, a full three-dimensional surface model is created using the geometry toolbox developed by Gagnon and Zingg known as Genair [24]. A breakdown of the planform geometry is given in Tables 1 and 2, with a definition for aircraft sections provided in Fig. 1. A visualization of the 3D model including winglets is shown in Fig. 2.

The outboard wing is given a dihedral of 3 degrees and the cabin-carrying portion of the aircraft is modelled without dihedral. The aircraft model also includes winglets that are matched to what is available on the TU Delft Flying V website [23]. Nacelles and pylons are not modelled on the aircraft. The geometry used to initialize the optimization uses SC(2)-0014 sections for the inboard portion of the aircraft, that is, up to the trailing edge kink in the planform (section II), to maintain sufficient thickness to house the cabin. For the outboard wing, starting at the leading edge kink (section III) up to the winglet (section IV), SC(2)-0012 sections are used. The winglet uses the SC(2)-0010 sections. The airfoil coordinates are obtained from [25]. For the initial geometry, airfoil shapes are linearly interpolated in the transition region between sections II and III.

A rectangular cross-section passenger cabin is considered as opposed to the ovoidal shape chosen by Faggiano et al. to give the optimizer further shaping freedom on the leading edge. The rectangular cabin is sized such that it is coincident with the oval defined by Faggiano et al. Eccentricities due to cockpit and mid-line cabin transition are ignored for simplicity. This study also explicitly models the cargo cabin as an extension outboard of the passenger cabin, with a cross-sectional width, perpendicular to the leading edge, of 5 m and a minimum height of 1.63 m, equivalent to that of a unit load device (ULD) [26]. Calculation of the total cargo volume available in the model agrees well with the required volume of 172.4 m^3 [7] and 14 ULD's per wing [23]. Figure 3a shows the model for the passenger and cargo cabin shape. In Fig. 3b, the cabin shape can be seen to protrude from the outer mold line (OML) of the baseline aircraft; this will be addressed during optimization.

The flight condition that the wide-body Flying V aircraft will be operated at throughout this study is the start of cruise condition. Faggiano et al. reported the aircraft mass at this point in cruise to be 200,000 kg [7]. At an altitude of 13,000 m, the aircraft lift coefficient is 0.26. Weight estimation of the wide-body is not performed in favour of using values provided by TU Delft. The center-of-gravity (CG) positions for aircraft designs investigated in this study are chosen rather than calculated. They are positioned to be some percentage of mean aerodynamic chord (MAC) ahead of the neutral point by the end of optimization to satisfy static margin requirements, consistent with [7].

B. Sizing of a Single-Aisle Equivalent Flying V Aircraft

To supplement the wide-body Flying V aircraft, the configuration is also modelled at the single-aisle size, which represents the largest market segment in the industry. Since there is no reference design for a Flying V aircraft in this class, the wide-body aircraft is sized down to provide a baseline geometry. The baseline wide-body Flying V aircraft is scaled down in all dimensions by its MAC, which decreases from 18 m for the wide-body to 10.8 m for the single-aisle variant via the following formula:

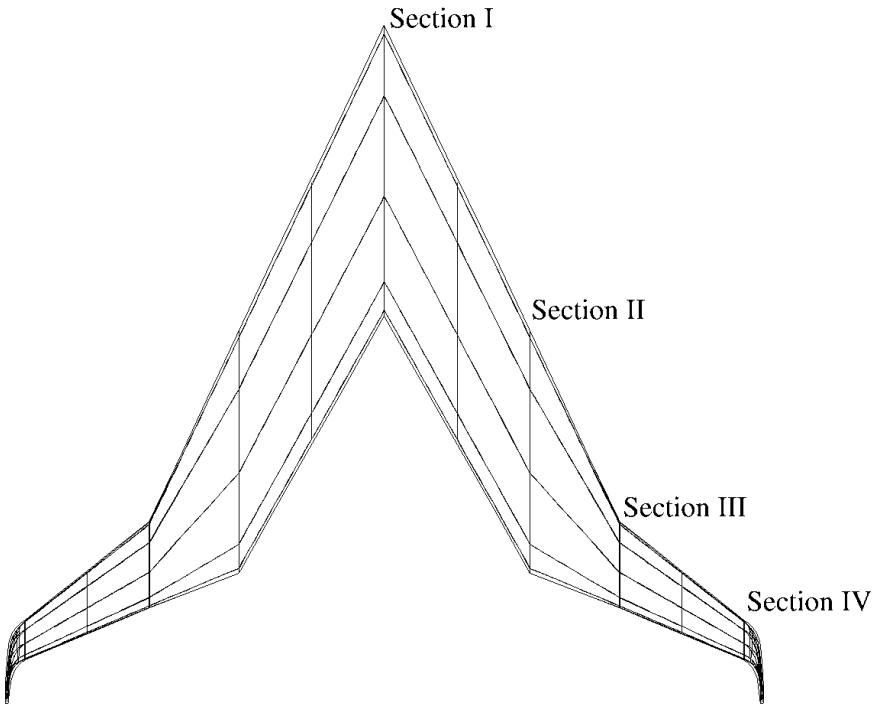

Fig. 1 Defining the four major sections of the aircraft planform definition.

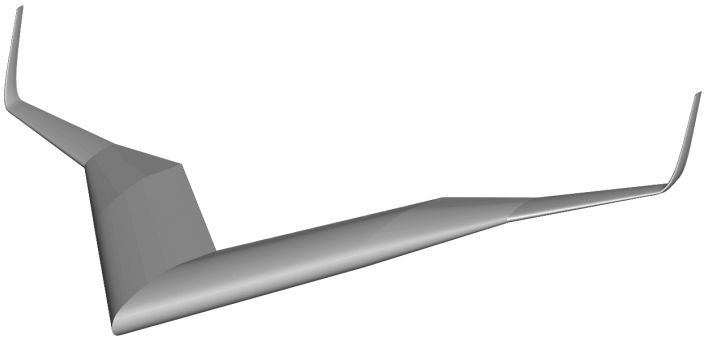

Fig. 2 Baseline Flying V 3D model produced by the Genair geometry toolbox.

$$L_{SA} = L_{WB}\left(\frac{A_{SA}}{A_{WB}}\right)^{0.5} \tag{1}$$

where L_{SA}, L_{WB}, A_{SA}, A_{WB} represent aircraft MAC and cabin floor area for the single-aisle and wide-body, respectively. Table 3 summarizes the cabin design quantities discussed above. The scaling also brings the aircraft's wing span close to compliance with Gate C constraints, which are typically imposed on single-aisle class aircraft. As this aircraft is sized to be significantly smaller than the wide-body, changes in optimal planform and cabin layout are expected. Optimizations

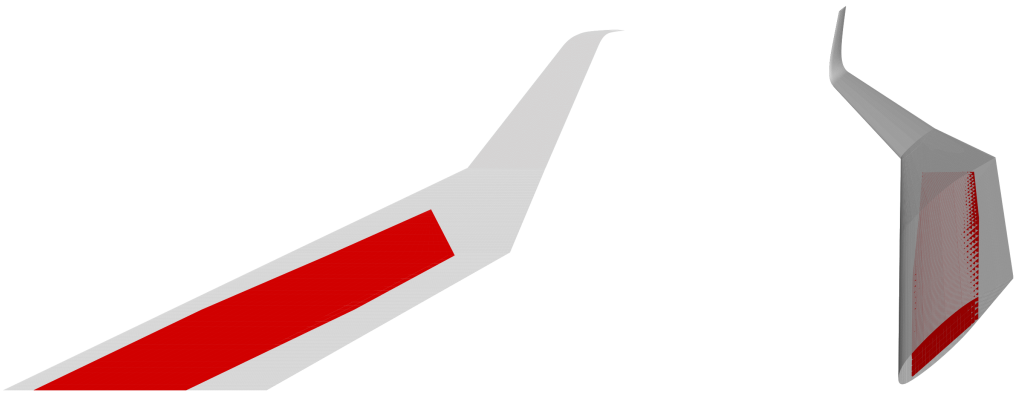

(a) Cabin shape within the aircraft planform. **(b) Cabin shape protruding from baseline aircraft OML.**

Fig. 3 Visualizations of the cabin within the baseline Flying V aircraft.

Table 3 Passenger and cargo cabin floor area and volume information [27, 28].

	Single-Aisle		Wide-body	
	Floor Area [m^2]	Volume [m^3]	Floor Area [m^2]	Volume [m^3]
Passenger	108.6	228.1	272.2	571.7
Cargo	32.8	37.4	120.3	172.4
Total	141.4	265.5	378.0	744.1

will include significant planform freedom unlike before, which will help determine the optimal cabin layout for a Flying V aircraft of this size.

C. Geometric Analysis of Flying V Planform Variations

To examine how the wetted area benefit of the Flying V aircraft changes with scale (single-aisle, wide-body, etc) and proportions (longer span, shorter chord, etc), a geometric investigation is undertaken. Historically, studies of this nature begin at the smallest aircraft size and add (plugs) to the planform to eventually obtain the largest aircraft. However, given that the baseline Flying V design is at the wide-body size, the use of deletions makes more sense. Two deletion fractions are used to scale the cabin-fitting portion of the aircraft:

- **Chordwise deletion fraction:** fraction of inboard chord (cabin-fitting portion of the aircraft) to be removed
- **Spanwise deletion fraction:** fraction of inboard span (cabin-fitting portion of the aircraft) to be removed

The outer-wing area is scaled to match the reduction of area experienced on the inboard portion of the aircraft as a result of the deletions. Note that negative deletion fractions represent an addition. The scheme is shown in Fig. 4.

A grid of spanwise deletion fractions ranging from -1 to 1 and chordwise deletion fractions of -0.5 to 0.5 is generated, for which contours of floor area (A_{floor}), wetted area-to-floor area ratio (S_{wet}/A), wetted aspect ratio (AR_{wet}), and maximum thickness-to-chord ratio (t/c_{max}) are plotted in Fig. 5. There are two cabin floor area contours at 141.4 m^2 and 378 m^2, which represent the floor area required by a single-aisle and wide-body aircraft, respectively. Wetted aspect ratio grows as the chord shrinks and span increases, while the wetted area-to-floor area ratio shrinks moving toward the top right of the plot. This suggests that planform-optimized designs should move toward the right on their respective floor area contours, i.e. in the direction of lower chord and higher span. One observation that the plot makes clear is how the maximum thickness-to-chord ratio grows with wetted aspect ratio, which may lead to shock formation. This will be investigated further when optimization results are obtained.

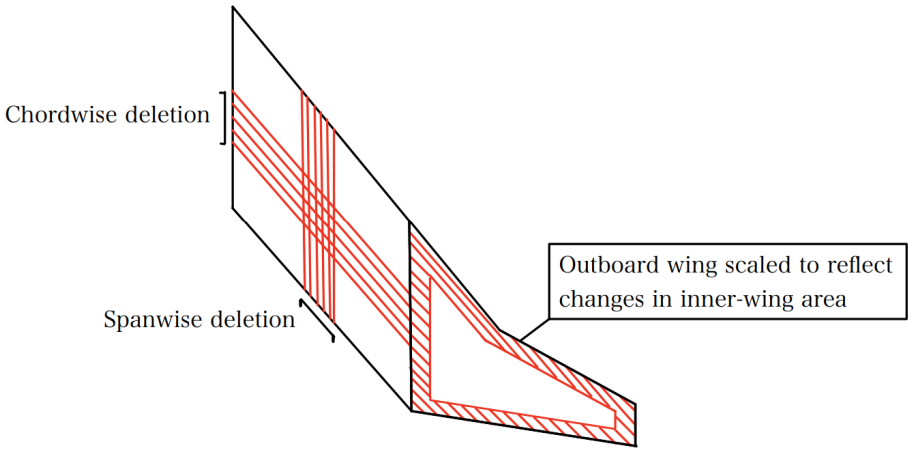

Fig. 4 Chordwise and spanwise deletion scheme.

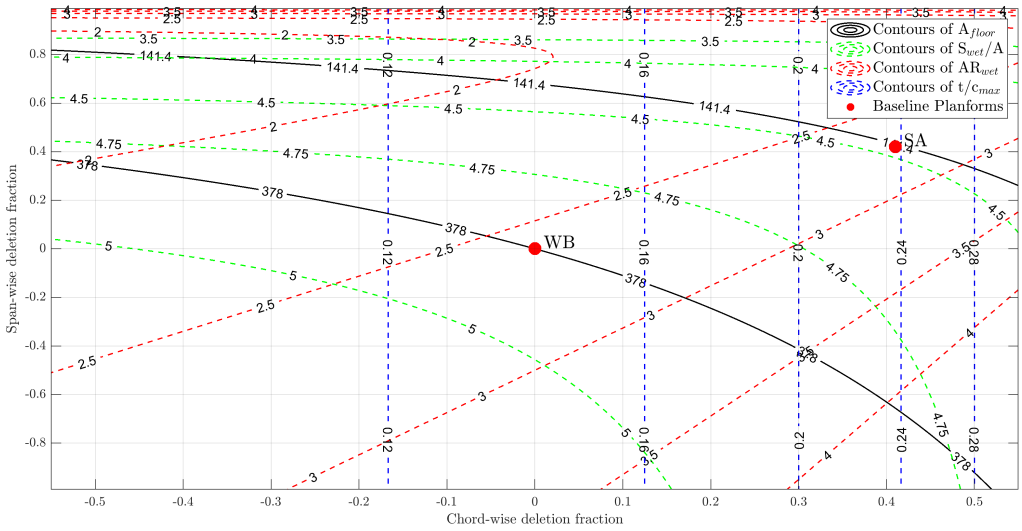

Fig. 5 Geometric analysis of the Flying V concept. Floor areas given in m^2.

IV. Optimization Problem Formulation

A. Wide-Body Flying V Aircraft

RANS-based aerodynamic shape optimization is performed on the Flying V aircraft at the start-of-cruise operating condition. The optimization objective is prescribed to be drag minimization subject to various aerodynamic and geometric constraints. Two driving aerodynamic constraints are the lift coefficient equality constraint and a trim constraint that dictates the pitching moment about the CG to be zero. Geometric constraints are mainly dictated by a minimum maximum thickness-to-chord ratio constraint of 8.5% on sections III and IV to prevent a structurally infeasible outboard wing [7] and a cabin shape constraint that requires the cabin floor and ceiling to be enclosed by the aircraft OML. With symmetric airfoils and untwisted wing sections, the starting aircraft will not satisfy the lift and geometric constraints. The wide-body optimizations are branched into planform-fixed and planform-free runs. While planform freedom allows for further exploration of the aircraft's aerodynamic optimum, the baseline planform is the product of considerations beyond aerodynamic efficiency [7], motivating planform-fixed optimization runs.

Table 4 Design variables and constraints for planform-fixed wide-body optimizations. Numbers in parentheses give the number of each variable or constraint.

Variables			Constraints	
$-3° \leq$	AoA (1)	$\leq 3°$	$0.085 \leq$	Maximum thickness-to-chord ratio (5)
$-15° \leq$	Twist (24)	$\leq 15°$		Cabin shape surface
$5\% \leq$	Shape (481)	$\leq 200\%$		$C_L = 0.26$
				$C_{M@CG} = 0$

1. Planform-Fixed Optimization Formulation

Even with the planform fixed, there are many design variables for the optimizer to work with in order to minimize drag. The angle-of-attack is a design variable with bounds of ±3 degrees, dictated by deck angle requirements. The wing is divided into 4 segments, the most inboard segment with a near-unity taper, the mid-span transition region, the outboard wing that is noticeably less swept than the two inboard segments, and the winglet. They have 5, 4, 5, and 11 span stations defined, respectively. There are 22 section variables available at each span station, split evenly between the lower and upper surfaces. The twist angle, which represents the rotation of the FFD volume cross-section about the local origin in the xz-plane, is free at all described span stations, except at the aircraft centerline. The range of twist angles at each span station is ±15 degrees. The pair of lower and upper surface section shape variables are allowed to vary from 5% to 200%, which represent a scaling of the vertical distance from the local origin to the position of a given FFD volume control point in the z-direction. The section shape variables are defined separately for each control point within the FFD volume. Table 4 presents the variables and constraints of the optimization. There are a total of 506 geometric design variables active during the optimization.

Additionally, using this problem formulation, an investigation is carried out to evaluate the performance sensitivity of the aircraft to CG positioning. Four positions are chosen to be investigated in this study in the vicinity of the baseline aircraft's neutral point: 1.76, 1.8, 1.825, and 1.85 mean aerodynamic chord (MAC) lengths from the nose, carrying names of CG1, CG2, CG3, and CG4, respectively. The initial aircraft's neutral point is located at 1.825 MAC lengths. This study is discussed in Section V. An additional aircraft will be optimized with a CG positioned such that the *resulting optimized aircraft* has a static margin of 6%. This aircraft will be referred to as WB PF Fixed.

2. Planform-Free Optimization Formulation

Planform-free optimizations are performed in two steps. First, to determine the aerodynamically optimal planform, a lift-to-drag ratio maximization is performed with no constraints on lift or pitching moment. Cabin airfoil maximum thickness and planform projected area constraints ensure that the cabin height is retained and floor area remains unchanged in the exploration of the optimal cabin layout. The optimization problem is summarized in Table 5, with chord length (three inner-most span stations) and axial control point position freedom, which allows for change in sectional span and sweep angles. The variables dX and dY represent axial control point deviations from their initial values in the x and y-directions, respectively. Bounds for axial control point movement are specified to facilitate exploration in the design space close to the starting geometry and aid convergence. They also constrain the inner-wing sweep angle, although this was not an active during optimizations. Similarly, bounds on dY constrain span, which are active as the optimized planform increases its span to the upper bound. Figure 6 displays the volume and axial curves. The black grid represents the FFD volume enclosing the aircraft and the green spheres represent axial control points, which are joined by green line segments.

The rest of the formulation follows the fixed-planform case. The inner-wing taper constraint ensures that the resultant aircraft retains the Flying-V shape. This formulation produces a Flying V aircraft with a reduced chord, sweep, and a larger span, agreeing with the direction suggested by the geometric analysis. The change in geometry is contrasted with the baseline planform in Fig. 7. The cabin layout that fits best into the new planform is the 3-2-3 passenger/aisle layout, representing a reduction in width from 3-4-3. A rectangular cabin is modelled to enclose the required volume and surface area as specified in Table 3 with a cabin width that corresponds to the chosen layout. The cabin height is stepped down to the height of a ULD (1.63 m for wide-bodies) for the outboard portion that is to carry cargo pallets. In-line with WB PF Fixed, the CG is positioned to produce a static margin of 6% for the optimized aircraft.

The second step, for which results will be presented, requires fitting the new cabin within the new aircraft and re-implementing the full range of constraints, with the goal of minimizing the deviations from the geometry that was

Table 5 Design variables and constraints for step one of planform-free wide-body optimizations. Numbers are the quantity of each variable or constraint.

Design Variables			Constraints	
$-3° \leq$	AoA (1)	$\leq 3°$	$0.085 \leq$	Maximum t/c - outboard wing (2)
$-15° \leq$	Twist (24)	$\leq 15°$	3.3 m $\leq$	Cabin airfoil thickness (5)
$5\% \leq$	Shape (481)	$\leq 200\%$		Fixed sectional area (4)
$50\% \leq$	Chord (3)	$\leq 200\%$	$0.833 \leq$	Inner wing taper ratio (1)
	$\|\|$ Axial dX, dY (14) $\|\|$	≤ 0.25 MAC		

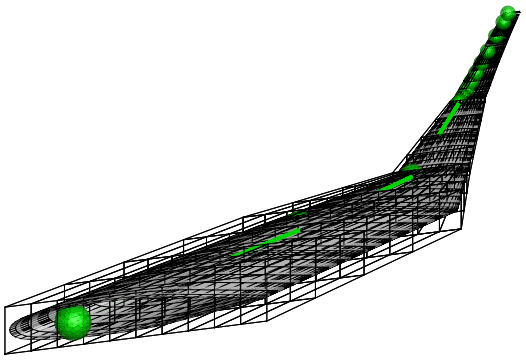

Fig. 6 Baseline Flying V aircraft FFD grid (black) and axial control points (green).

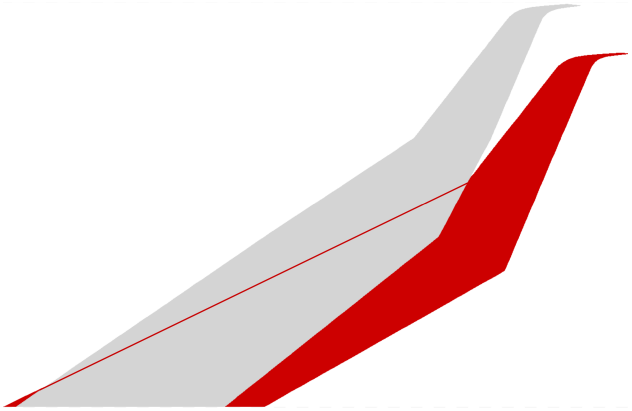

Fig. 7 Comparison of the optimized planform (grey) with the baseline planform (red).

determined in the previous step. The eventual fitting compromise is to grow the OML of the optimized aircraft such that the new MAC is 5% bigger, which will demand a lower design C_L for the same internal weight. However, this allows for the retention of the new planform shape. The problem formulation as shown in Table 4 is then repeated albeit with a different lift coefficient. The weight of this aircraft is the same as that used for WB PF Fixed. The planform-free design will be referred to as WB PF Free. Table 6 displays the resultant start-of-cruise C_L for WB PF Free in comparison to WB PF Fixed.

Table 6 C_L values for wide-body optimizations.

Design	Altitude [m]	MTOW [kg]	Planform Area [m^2]	C_L
WB PF Fixed	13,000	225,000	883.3	0.26
WB PF Free	13,000	225,000	970.5	0.24

Table 7 Design variables and constraints for step two of single-aisle optimizations. Numbers are the quantity of each variable or constraint.

Variables			Constraints	
$-3^\circ \leq$	AoA (1)	$\leq 3^\circ$	$0.085 \leq$	Maximum thickness-to-chord ratio (2)
$-15^\circ \leq$	Twist (24)	$\leq 15^\circ$		Cabin shape surfaces (2)
$5\% \leq$	Shape (481)	$\leq 200\%$		$C_L = 0.26$ (1)
$50\% \leq$	Chord (3)	$\leq 200\%$		$C_{M@CG} = 0$ (1)
	$\|\|$ Axial dX, dY (14) $\|\|$	≤ 0.25 MAC		

Table 8 Mass breakdown of the single-aisle Flying V compared to the Airbus A320.

Aircraft	OEW [kg]	MFW [kg]	MTOW [kg]
A320	42,100	20,400	79,000
Single-Aisle Flying V	37,000	17,500	71,000

B. Single-Aisle Flying V Aircraft

Unlike the wide-body Flying V aircraft, no reference design currently exists for the equivalent aircraft at the single-aisle size to the authors' knowledge. As a result, all optimizations are performed with full planform freedom. The starting geometry for optimizations is the scaled down baseline wide-body planform as discussed in Section III.B. The two-step process outlined in Section IV.A.2 for the planform-free optimization of the wide-body is roughly repeated for the single-aisle Flying V aircraft. Lift-to-drag ratio maximization is performed at a Mach number of 0.78, which is the nominal cruise speed for single-aisle aircraft [27], to obtain the starting geometry for the second step. Design variables and constraints for this step align with what was previously shown in Table 5. While the result of the first step is seen to resemble the wide-body planform closely, cabin fitting trials suggest deviations away from that shape. The initial geometry for the second optimization must be enlarged such that the new MAC is 10% larger to accommodate a 3-3 cabin layout for the single-aisle Flying V aircraft. More importantly, step two in this study is performed differently than it is for the wide-body planform-free optimizations, namely, the planform is free to better facilitate the cabin fitting process. This relaxation was not required for step two of the wide-body planform-free optimizations. Table 7 describes the specific design variables and constraints in optimization formulation. Additionally, the cargo section of the cabin is modelled with a ULD height of 1.14 m, which is the norm for single-aisle pallets [28], allowing for thinner outboard cabin airfoils. Both single-aisle aircraft have CG's positioned such that the optimized aircraft has a static margin of approximately 6%.

A weight estimate for the single-aisle Flying V aircraft is calculated using the empirical method presented by TU Delft [10]. The weight estimate depends on the lift-to-drag ratio, so iterations are required to obtain the weight estimate corresponding to the final aircraft lift-to-drag ratio. The weight estimate is broken down and compared to the Airbus A320neo in Table 8. The single-aisle aircraft is investigated at two altitudes. The Flying V aircraft tends to be more efficient at higher cruise altitudes; however, single-aisle aircraft missions often involve a relatively short cruise segment, so this benefit can be outweighed by the increase in fuel needed to climb to the higher altitude. The altitudes selected for each optimization are 10,973 m and 13,411 m, which correspond to 36,000 ft and 44,000 ft, respectively. The low and high altitude single-aisle Flying V designs will be referred to as SA FL360 and SA FL440, respectively. Table 9 displays the resultant start-of-cruise C_L values for the two designs. The reduction in MTOW seen for SA FL440 is due to the increased aircraft efficiency at the higher altitude, reducing fuel weight as well as its associated structural weight

Table 9 C_L values for single-aisle optimizations.

Design	Altitude [m]	MTOW [kg]	Planform Area [m^2]	C_L
SA FL360	10,973	71,000	416.3	0.16
SA FL440	13,411	68,000	416.3	0.22

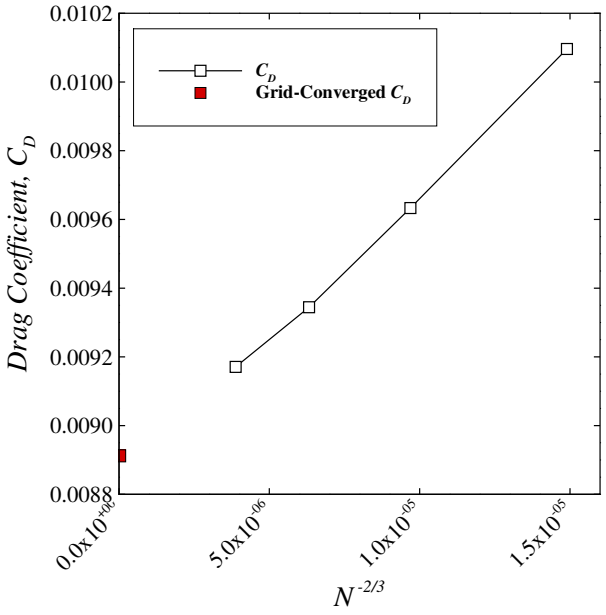

Fig. 8 Baseline wide-body Flying V aircraft grid convergence study at Mach 0.85 and $C_L = 0.26$. N represents the number of grid nodes.

C. Grid Convergence

The Flying V aircraft is optimized using grids of 1.7×10^6 nodes. Final force and moment coefficients are determined by performing a grid convergence study on the optimized design. For each design, three additional grids with two, four, and eight times the number of nodes on the grid described above are created and used for flow evaluation. Richardson extrapolation is performed to estimate grid-converged performance. All performance results presented are Richardson extrapolated estimates. Figure 8 shows the convergence study performed on the baseline geometry, with the connected black-outlined marker representing flow evaluation results and the red marker representing the Richardson extrapolated drag coefficient. This study is performed at constant C_L.

D. Optimization Convergence

Optimization convergence is measured in terms of the merit function, which is effectively the objective function once the constraints are satisfied. Optimality represents the gradient of an augmented objective and feasibility quantifies the degree to which the constraints are satisfied. All optimizations presented are continued until the merit function attains a plateau, while the optimality and feasibility drop at least three and six orders, respectively. Figure 9 shows the optimization history associated with the CG1 design, highlighting the points discussed above.

V. Wide-Body Flying V Results and Discussion

This section will discuss the results obtained from optimization runs performed on the wide-body size Flying V aircraft. Looking first at the fixed-planform optimization runs, minimal solution change is seen moving from the forward-most to the aft-most CG position. Consequently, only CG1 and CG4 solution visualizations are shown. For CG1, the spanwise lift distribution is seen in Fig. 10a. With a forward CG, it makes sense to see an equal increase in lift at inboard sections to the decrease seen in the cabin-to-wing transition region as the optimizer works to trim the

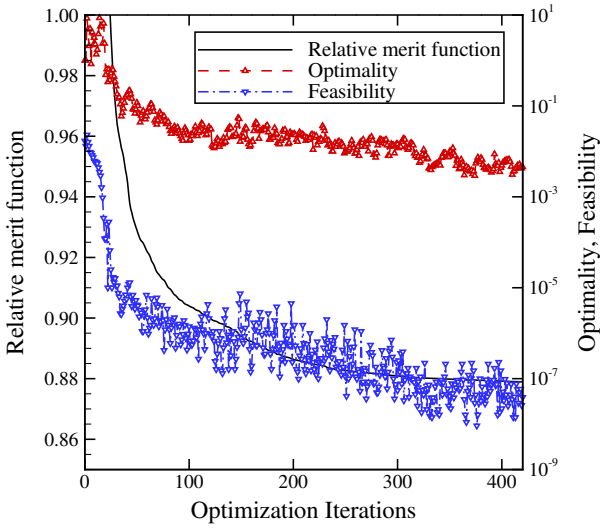

Fig. 9 Optimization history for the CG1 Flying V aircraft optimization case.

Table 10 Performance of optimized aircraft at the start of cruise.

Design	AoA [deg]	C_L [-]	C_D [−]	C_L/C_D [-]	Resulting K_n [% MAC]
CG1	3.00	0.26	0.0104	24.9	8.8
CG2	3.00	0.26	0.0101	25.6	5.1
CG3	3.00	0.26	0.0101	25.8	3.5
CG4	3.00	0.26	0.0100	26.0	1.7

aircraft. The surface pressure distribution is shown in Fig. 10b. Sectional pressure distributions and airfoils are shown in Fig. 10c at 6 span stations: the centerline (section I), start of transition region (section II), end of transition region (section III), and three positions along the outboard wing. The geometry is seen to be shock free with the exception of some weak shocks in the wing-winglet junction. Fore-loading is a prevalent trend among the sections, excluding the centerline and outboard stations, which show significant aft loading. Moving outwards toward the winglets, there is a noticeable reduction in leading-edge radius starting at 45% span, which makes sense as the cabin no longer drives shaping at that point. This aircraft accounts for the shape of the cargo hold outboard of the passenger cabin, so it is expected for the optimizer to encounter difficulties reducing section thickness in the transition region without violating the shape constraint. When comparing to Faggiano et al., their fore-loading is far less pronounced on mid-wing sections and outboard wing sections feature a noticeable hook near the trailing edge [7]. Their optimizer is likely exploiting the Euler solver's inability to detect separation to have steeper adverse pressure gradients at the trailing edge of their airfoils.

Inspecting CG4, which is the aircraft with the aft-most CG, the reduction in fore-loading in comparison to CG1 is visible in Fig. 11a, as the spanwise lift distribution shows greater lift generation up to the wing-transition region than what is seen in CG1's lift distribution. The aft CG position has resulted in CG4 carrying more load close to the winglet and less load on the inner wing, moving the loading back as expected. Despite that, the shocks previously seen on the inside of CG1's winglet are eliminated on CG4, and the region of low pressure on the leading edge of the aircraft has been reduced considerably as seen in Fig. 11b, showing a smaller blue-coloured region. Figure 11c shows reduced pressure peaks on the inboard aircraft sections and flatter airfoils, especially at the centerline, which makes sense, as trimming becomes easier with the aft CG. The CG4 aircraft is calculated to have a static margin of 1.71% MAC, which marks a 7% MAC reduction from CG1. A commonality among all optimized aircraft is the maxed out cruise angle of attack of 3 degrees. Table 10 compares the performance of the four designs. From CG1 to CG4, a 4.4% increase in lift-to-drag ratio can be observed. Figure 12 depicts the trade-off in performance seen across the designs discussed. The Flying V presented by Faggiano et al. sought and achieved a static margin of 6% MAC. This margin is replicated by WB PF Fixed, shown as a red point in Fig. 12, attaining a lift-to-drag ratio of 25.5.

Turning to the results produced by WB PF Free, Fig. 13a shows a smoother spanwise lift distribution. The area of

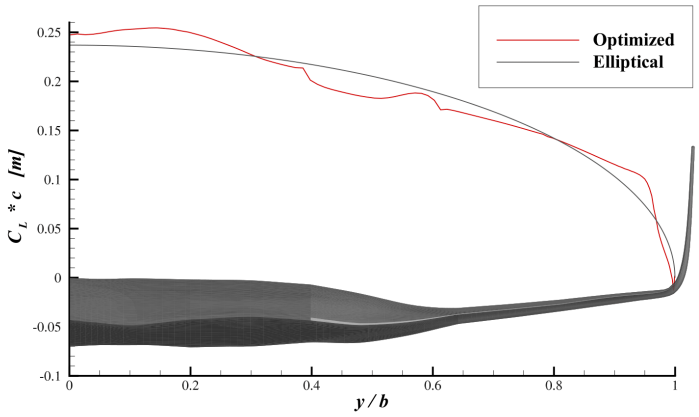

(a) Spanwise lift distribution

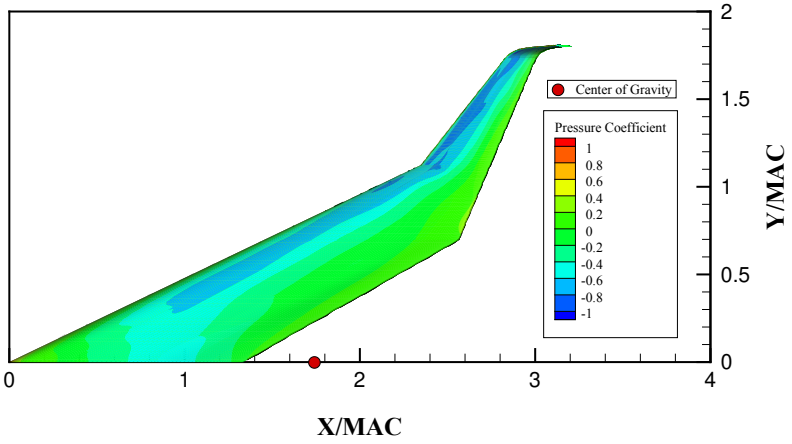

(b) Surface pressure distribution

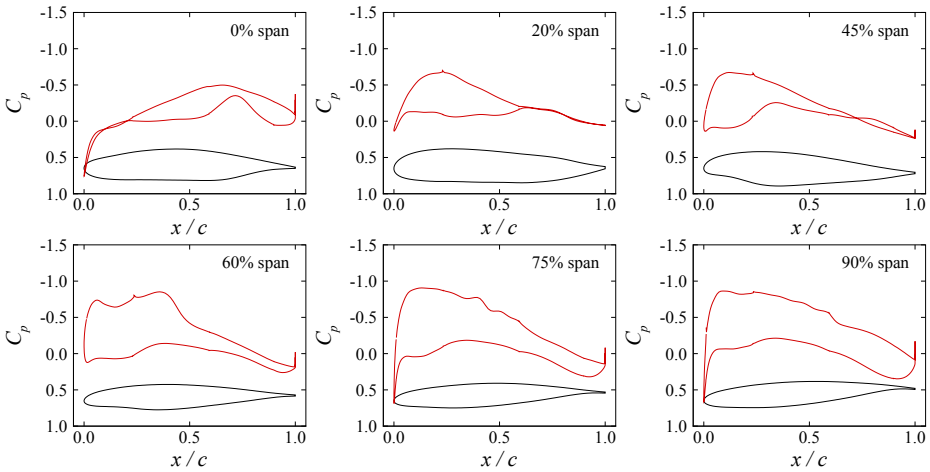

(c) Sectional pressure distributions

Fig. 10 Solution information for the CG1 Flying V aircraft.

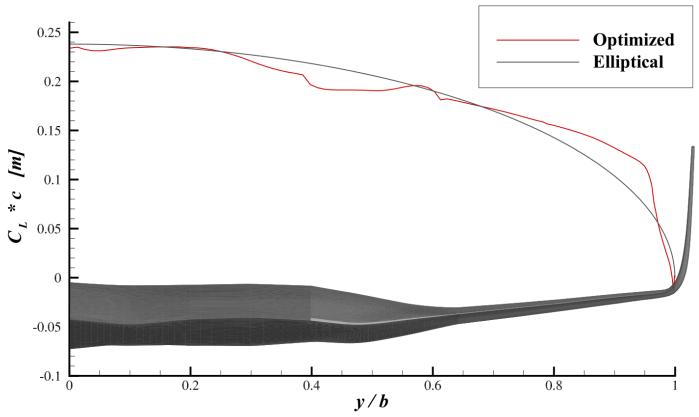

(a) Spanwise lift distribution

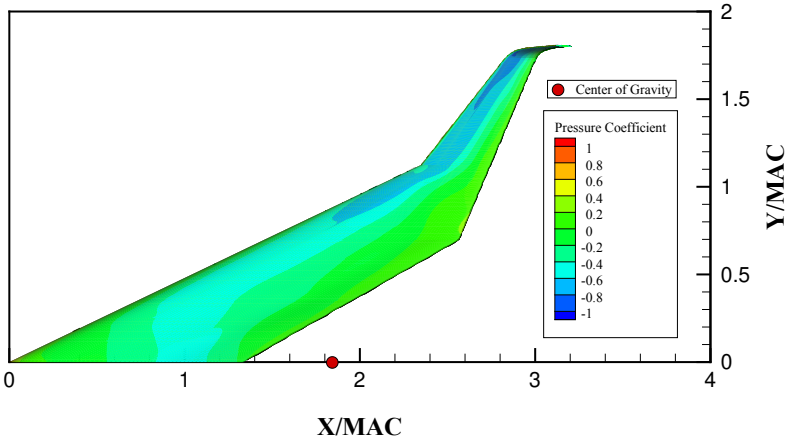

(b) Surface pressure distribution

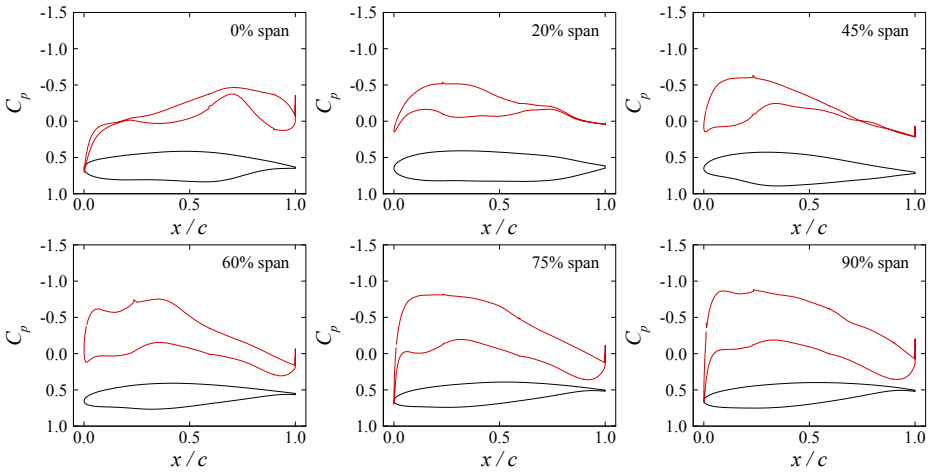

(c) Sectional pressure distributions

Fig. 11 Solution information for the CG4 Flying V aircraft.

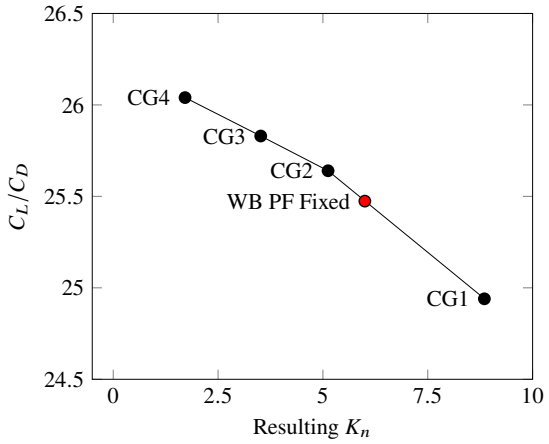

Fig. 12 Lift-to-drag ratio plotted against static margin variations.

Table 11 Performance of optimized wide-body aircraft at the start of cruise.

Design	Altitude [m]	AoA [deg]	C_L [-]	C_D [−]	C_L/C_D [-]
WB PF Fixed	13,000	3.00	0.26	0.0101	25.5
WB PF Free	13,000	3.00	0.24	0.0089	27.0

low pressure on the outer-wing is completely eliminated for this aircraft when compared to WB PF Fixed, which had a fixed planform during optimization, as shown in Fig. 13b. Section shapes displayed in Fig. 13c resemble results from CG1 and CG4 for the inboard and outboard sections, while the transition region shows thicker airfoils. No shocks are seen across the aircraft. Table 11 breaks down the performance of the two wide-body aircraft with a 6% static margin. WB PF Free has a 6% greater lift-to-drag ratio. Figure 14 displays the aerodynamic properties of the two aircraft, both of which would benefit from a higher cruise altitude. Figure 15 shows how the drag rises with increased Mach number.

VI. Single-Aisle Flying V Results and Discussion

This section presents the results obtained for the two single-aisle Flying V designs. Comparing the solution information presented in Fig. 16 and 17, the only difference in results can be attributed to the difference in cruise altitudes, which means that SA FL440 operates at a higher lift coefficient. Looking at the geometry for both aircraft, it can be observed that the taper ratio is further away from unity than the optimized wide-body geometry shown in grey in Fig. 7 due to the longer root chord. The initial airfoil thickness was insufficient to wrap the cabin at the leading and trailing edges, prompting the extension. Compared to the wide-body aircraft, both single-aisle designs have significantly thicker airfoils to accommodate the standard cabin height of 2.1 m, which presents itself as an important design driver. The immediate thinning of the airfoils at the boundary between the passenger and cargo cabins (step change in height) further supports that claim. Despite the unusually thick airfoils, both single-aisle aircraft exhibit no shock formation. Table 12 summarizes the aerodynamic performance of the two single-aisle Flying V aircraft. A signficant performance difference can be seen in favour of SA FL440, with a 17% reduction in drag and a 14% increase in lift-to-drag ratio. For context, air density drops by 32% going from 10,973 m to 13,411 m.

When looking at the aerodynamic performance of both aircraft across a range of lift-coefficients shown in Fig. 18, the curve associated with SA FL360 sits higher than SA FL440, as it operates at an angle of attack that exceeds the deck angle of three degrees imposed during optimization. For example, SA FL360 operates at an angle of attack of 3.6 degrees to produce the same lift coefficient as SA FL440, which operates at 3 degrees, constrained by deck angle requirements. On a separate note, the lift-coefficient at which SA FL360 operates is too low to be aerodynamically efficient in comparison to SA FL440. Similar to the wide-body case, both single-aisle aircraft attain their maximum aerodynamic performance operating at a cruise lift coefficient of above 0.3, reaffirming the inherent preference of the Flying V aircraft to fly at high altitudes. Drag divergence for both single-aisle Flying V aircraft is shown in Fig. 19.

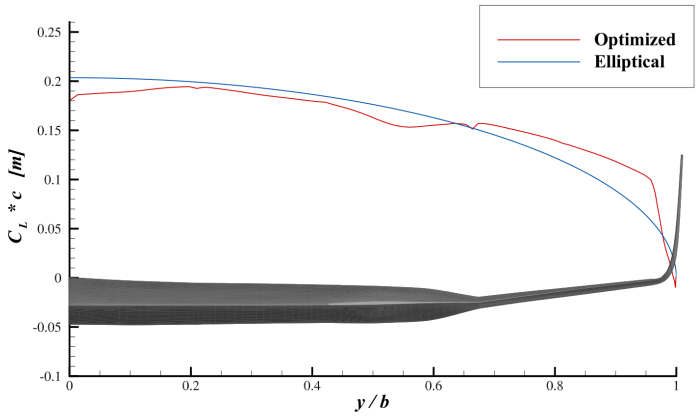

(a) Spanwise lift distribution

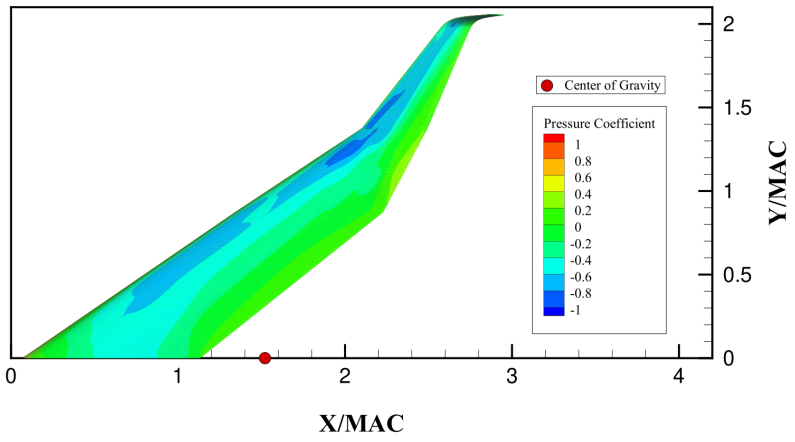

(b) Surface pressure distribution

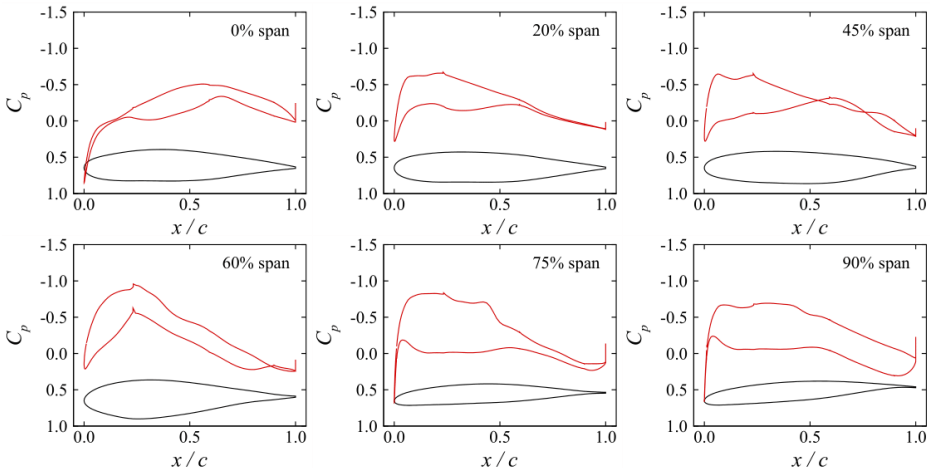

(c) Sectional pressure distributions

Fig. 13 Solution information for WB PF Free Flying V aircraft.

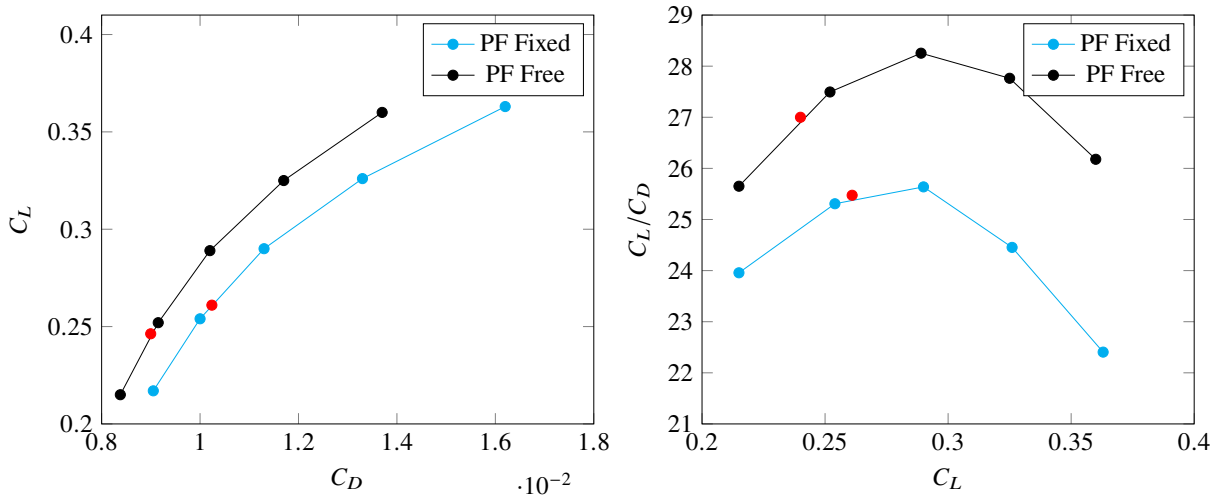

(a) Drag polar **(b) Maximum C_L/C_D vs C_L**

Fig. 14 Aerodynamic properties of the wide-body Flying V aircraft. The red symbols represent the optimization operating point for each aircraft.

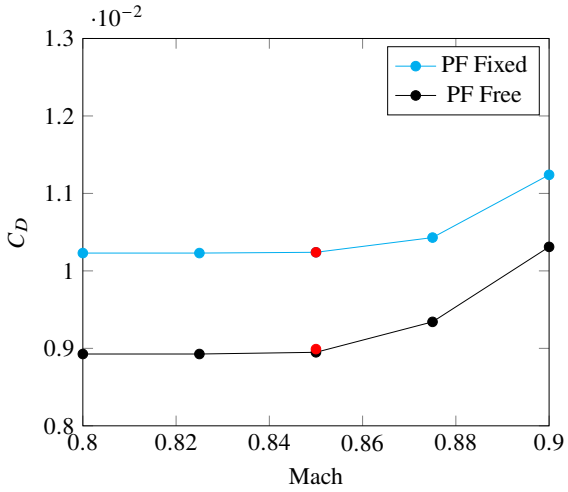

Fig. 15 Wide-body drag divergence plot. The red symbols represent the optimization operating point for each aircraft.

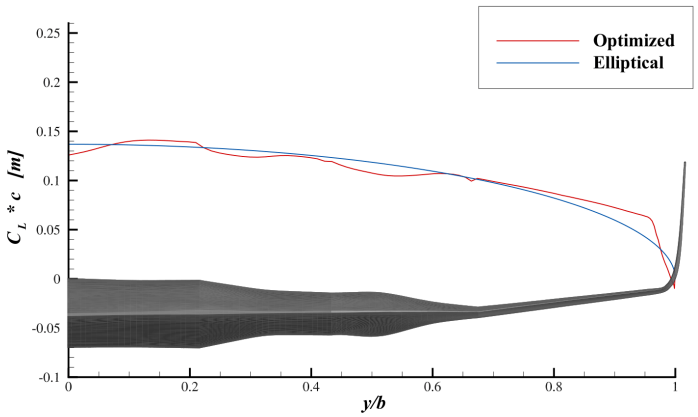

(a) Spanwise lift distribution

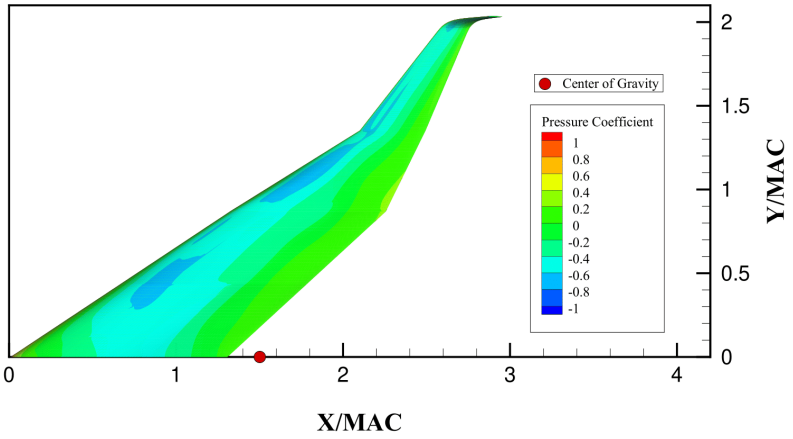

(b) Surface pressure distribution

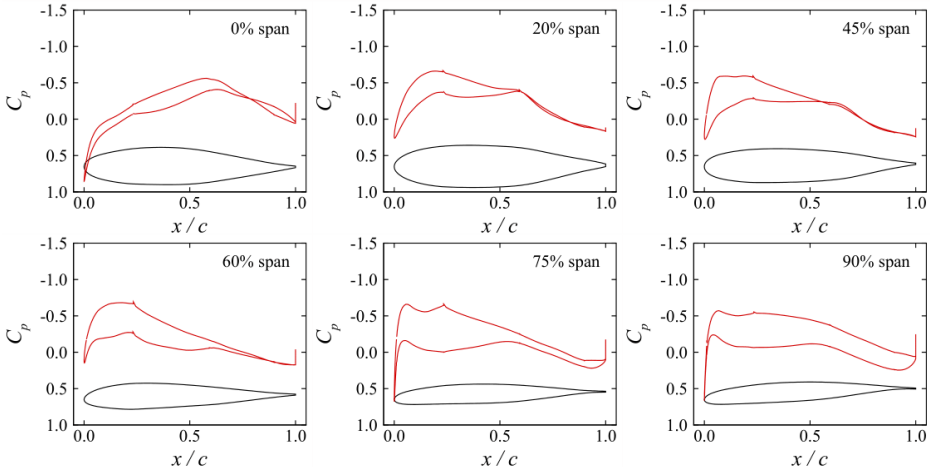

(c) Sectional pressure distributions

Fig. 16 Solution information for the SA FL360 Flying V aircraft.

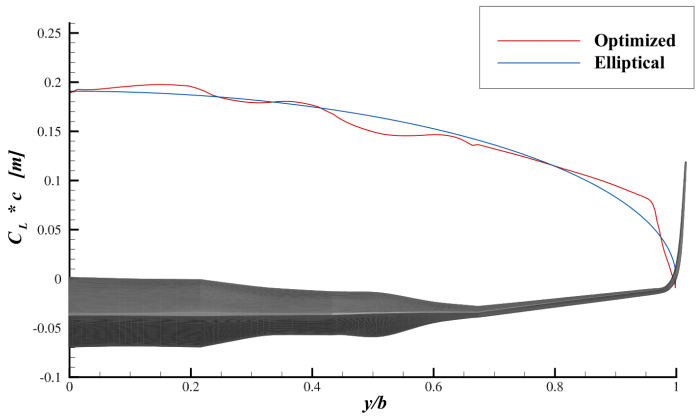

(a) Spanwise lift distribution

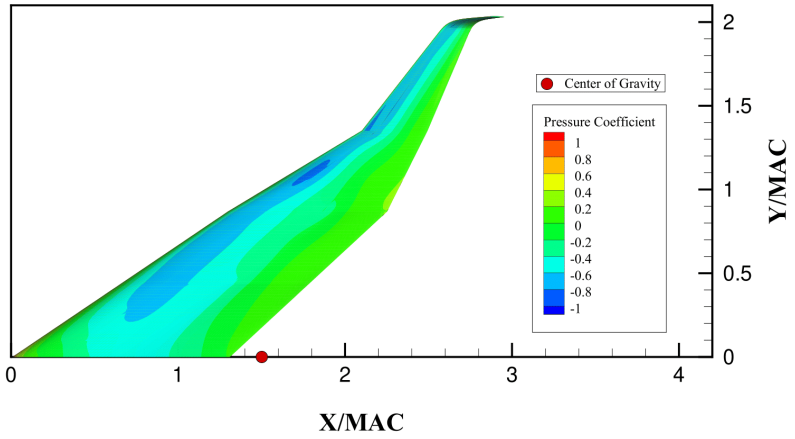

(b) Surface pressure distribution

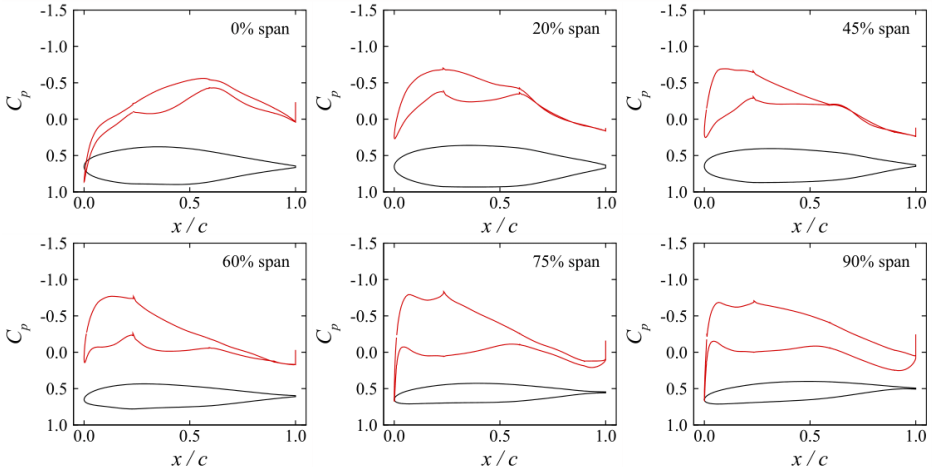

(c) Sectional pressure distributions

Fig. 17 Solution information for the SA FL440 Flying V aircraft.

Table 12 Performance of optimized single-aisle aircraft at the start of cruise.

Design	Altitude [m]	AoA [deg]	C_L [-]	C_D [−]	C_L/C_D [-]	D [N]
SA FL360	10,973	2.82	0.16	0.0077	20.4	30,900
SA FL440	13,411	3.00	0.22	0.0093	23.2	25,600

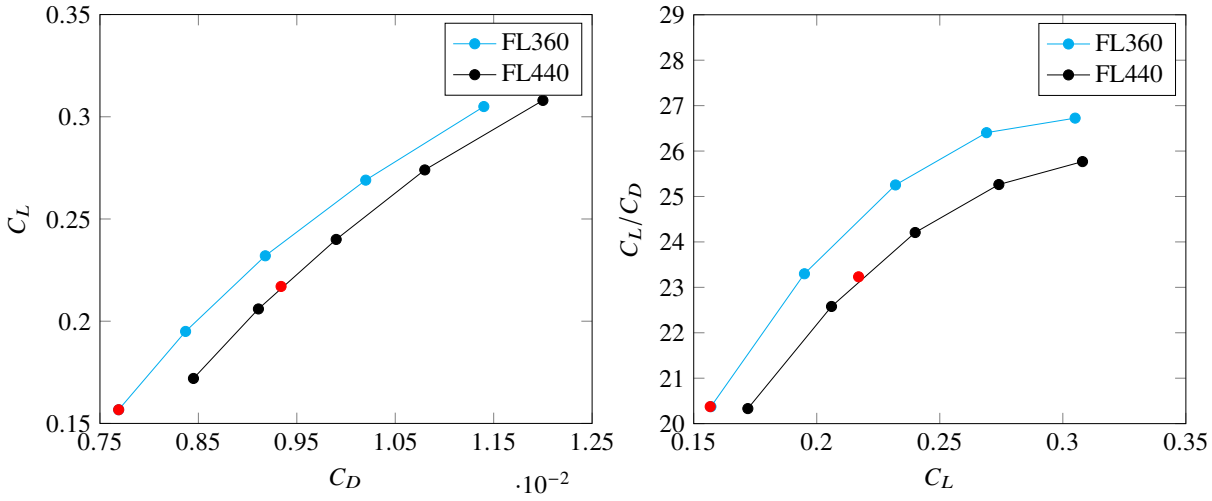

(a) Drag polar **(b) Maximum C_L/C_D vs C_L**

Fig. 18 Aerodynamic properties of the single-aisle Flying V aircraft. The red symbols represent the optimization operating point for each aircraft.

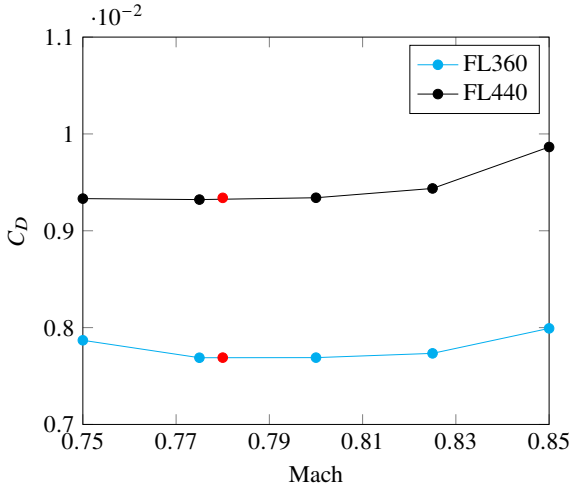

Fig. 19 Single-aisle drag divergence plot. The red symbols represent the optimization operating point for each aircraft.

VII. Conclusions

The aerodynamic performance of the Flying V aircraft configuration was investigated using RANS-based aerodynamic shape optimization in the wide-body and single-aisle classes, representing the two largest market segments in commercial aviation. The initial aircraft geometry was chosen to match the planform developed by Faggiano et al. [7], which was then optimized to minimize drag subject to lift and trim constraints at the start-of-cruise operating point. Drag contributions associated with nacelles, pylons, and excrescences are not considered.

At the wide-body level, planform-fixed optimization with freedom in shape and twist subject to a cabin shape

constraint, produces an aircraft with a lift-to-drag ratio of 25.5 at 13,000 m and a static margin of 6%. The optimized aircraft produced by Faggiano et al. has a lift-to-drag ratio of 23.7 with the same operating conditions and static margin. Performance figures are comparable when considering their inclusion of nacelle and pylon drag contributions. The performance impact of static margin variations was studied using the preceding problem formulation over a range of 2% to 9% MAC. A 4.2% increase in lift-to-drag ratio is seen when reducing the margin from 9% to 2%, with nearly three quarters of the improvement being realized by relaxing the margin to 5%. Freedom in planform variables chord, span, and sweep allowed the optimizer to design an aircraft with a lift-to-drag ratio of 27, representing a 6% improvement. Despite a cruise Mach number of 0.85, the Flying V aircraft is free of strong shocks, which was a concern highlighted by Faggiano et al. The planform-free optimization increased the aircraft's span while reducing the chord and sweep, leading to a cabin layout of 3-2-3, which is narrower than the 3-4-3 layout of the baseline geometry.

Optimizations at the single-aisle size are all performed with planform freedom, as there is no reference planform for a Flying V aircraft in this class. After selecting a 3-3 cabin layout based on exploratory optimizations, an appropriate optimization formulation was applied to design single-aisle Flying V aircraft flying at 10,973 m and 13,411 m with a static margin of 6%. The high-altitude design has a lift-to-drag ratio of 23.2, while the low-altitude single-aisle Flying V produced a lift-to-drag ratio of 20.4, again demonstrating the Flying V aircraft's affinity for flying at high altitude.

The primary conclusions of the present work are as follows:

1) Performance estimates based on RANS-based aerodynamic shape optimization corroborate the predictions of the Delft group [7].
2) RANS-based aerodynamic shape optimization produced geometries with very low wave drag and lift-to-drag ratios competitive with some of the best unconventional configurations.
3) The Flying V concept can perform well in the single-aisle class, although its performance is more impressive in the wide-body class.

VIII. Acknowledgements

This work was partially funded by the Natural Sciences and Engineering Research Council (NSERC), Transport Canada, and the University of Toronto Institute for Aerospace Studies. Computations were performed on the Niagara supercomputer at the SciNet High Performance Computing (HPC) Consortium, which is a part of Compute Canada. The authors gratefully acknowledge the input and support provided by Aiden Gray.

References

[1] Torenbeek, E., "Blended Wing Body and All-Wing Airliners," *European Workshop on Aircraft Design Education (EWADE)*, 2007.

[2] R Martinez-Val and E Perez and J Puertas and J Roa, "Optimization of planform and cruise conditions of a transport flying wing," *Proceedings of the Institution of Mechanical Engineers, Part G: Journal of Aerospace Engineering*, Vol. 224, No. 12, 2010, pp. 1243–1251. https://doi.org/10.1243/09544100JAERO812.

[3] Blain, L., "Boeing to build braced-wing airliner, shooting for 30% efficiency gain," , Jan 2023. URL https://newatlas.com/aircraft/boeing-nasa-truss-braced/.

[4] Blain, L., "JetZero aims to put ultra-efficient blended-wing jet in service by 2030," , May 2023. URL https://newatlas.com/aircraft/jetzero-blended-wing/.

[5] Bolsunovsky, A., Buzoverya, N., Gurevich, B., Denisov, V., Dunaevsky, A., Shkadov, L., Sonin, O., Udzhuhu, A., and Zhurihin, J., "Flying wing—problems and decisions," *Aircraft Design*, Vol. 4, No. 4, 2001, pp. 193–219. https://doi.org/https://doi.org/10.1016/S1369-8869(01)00005-2.

[6] "B2 Spirit," *US Air Force*, retrieved 5 February 2023. URL https://www.af.mil/About-Us/Fact-Sheets/Display/Article/104482/b-2-spirit/.

[7] Faggiano, F., Vos, R., Baan, M., and Dijk, R., "Aerodynamic Design of a Flying V Aircraft," AIAA Paper 2017-3589, 2017. https://doi.org/10.2514/6.2017-3589.

[8] Benad, J., "The Flying V - A new Aircraft Configuration for Commercial Passenger Transport," 2015, pp. 1–8. https://doi.org/10.25967/370094, deutscher Luft- und Raumfahrtkongress 2015, Rostock ; Conference date: 22-09-2015 Through 24-09-2015.

[9] Benad, J., and Vos, R., "Design of a Flying V Subsonic Transport," *ICAS 2022*, International Council of the Aeronautical Sciences (ICAS), Sweden, 2022. https://doi.org/https://www.icas.org/ICAS_ARCHIVE/ICAS2022/data/preview/ICAS2022_0358.htm.

[10] Oosterom, W., and Vos, R., *Conceptual Design of a Flying-V Aircraft Family*, AIAA AVIATION 2022-3200, 2022. https://doi.org/10.2514/6.2022-3200, URL https://arc.aiaa.org/doi/abs/10.2514/6.2022-3200.

[11] Le Moigne, A. L., and Qin, N., "Aerofoil profile and sweep optimisation for a blended wing-body aircraft using a discrete adjoint method," *The Aeronautical Journal*, Vol. 110, No. 1111, 2006, p. 589–604. https://doi.org/10.1017/S0001924000001457.

[12] Lyu, Z., and Martins, J. R. R. A., "Aerodynamic Design Optimization Studies of a Blended-Wing-Body Aircraft," *Journal of Aircraft*, Vol. 51, No. 5, 2014, pp. 1604–1617. https://doi.org/10.2514/1.C032491.

[13] Reist, T. A., and Zingg, D. W., "High-Fidelity Aerodynamic Shape Optimization of a Lifting-Fuselage Concept for Regional Aircraft," *Journal of Aircraft*, Vol. 54, No. 3, 2017, pp. 1085–1097. https://doi.org/10.2514/1.C033798.

[14] Reist, T. A., Zingg, D. W., Rakowitz, M., Potter, G., and Banerjee, S., "Multifidelity Optimization of Hybrid Wing–Body Aircraft with Stability and Control Requirements," *Journal of Aircraft*, Vol. 56, No. 2, 2019, pp. 442–456. https://doi.org/10.2514/1.C034703.

[15] Chau, T., and Zingg, D. W., "Aerodynamic Optimization and Fuel Burn Evaluation of a Transonic Strut-Braced-Wing Single-Aisle Aircraft," *Journal of Aircraft*, 2023, pp. 1–21. https://doi.org/10.2514/1.C037158, URL https://doi.org/10.2514/1.C037158.

[16] van Luijk, N., and Vos, R., "Constrained Aerodynamic Shape Optimisation of the Flying V Outer Wing," *AIAA AVIATION 2023 Forum*, American Institute of Aeronautics and Astronautics Inc. (AIAA), United States, 2023. https://doi.org/https://doi.org/10.2514/6.2023-3250, aIAA AVIATION 2023 Forum ; Conference date: 12-06-2023 Through 16-06-2023.

[17] Osusky, M., and Zingg, D. W., "Parallel Newton–Krylov–Schur Flow Solver for the Navier–Stokes Equations," *AIAA Journal*, Vol. 51, No. 12, 2013, pp. 2833–2851. https://doi.org/10.2514/1.J052487.

[18] Gagnon, H., and Zingg, D., "Two-Level Free-Form and Axial Deformation for Exploratory Aerodynamic Shape Optimization," *AIAA Journal*, Vol. 53, 2015, pp. 1–12. https://doi.org/10.2514/1.J053575.

[19] Gill, P. E., Murray, W., and Saunders, M. A., "SNOPT: An SQP Algorithm for Large-Scale Constrained Optimization," *SIAM Journal on Optimization*, Vol. 12, No. 4, 2002, pp. 979–1006. https://doi.org/10.1137/S1052623499350013.

[20] Osusky, L., Buckley, H., Reist, T., and Zingg, D., "Drag Minimization Based on the Navier–Stokes Equations Using a Newton–Krylov Approach," *AIAA Journal*, Vol. 53, 2015, pp. 1555–1577. https://doi.org/10.2514/1.J053457.

[21] Chau, T., and Zingg, D. W., "Aerodynamic Design Optimization of a Transonic Strut-Braced-Wing Regional Aircraft," *Journal of Aircraft*, Vol. 59, No. 1, 2022, pp. 253–271. https://doi.org/10.2514/1.C036389.

[22] Reist, T. A., Koo, D., Zingg, D. W., Bochud, P., Castonguay, P., and Leblond, D., "Cross Validation of Aerodynamic Shape Optimization Methodologies for Aircraft Wing-Body Optimization," *AIAA Journal*, Vol. 58, No. 6, 2020, pp. 2581–2595. https://doi.org/10.2514/1.J059091, URL https://doi.org/10.2514/1.J059091.

[23] "Flying-V," *TU Delft*, retrieved 10 October 2022. URL https://www.tudelft.nl/lr/flying-v.

[24] Gagnon, H., and Zingg, D. W., *Geometry Generation of Complex Unconventional Aircraft with Application to High-Fidelity Aerodynamic Shape Optimization*, AIAA Paper 2013-2850, 2013. https://doi.org/10.2514/6.2013-2850.

[25] Selig, M. S., "Airfoil Coordinate Database by Michael S. Selig," , retrieved 10 October 2022. URL https://m-selig.ae.illinois.edu/ads/coord_database.html.

[26] "Aircraft Container Sizes," *Active Freight*, retrieved 20 January 2023. URL https://www.activfreight.com.au/customer-resources/aircraft-container-sizes/.

[27] Reist, T. A., "Scaling of Hybrid Wing-Body-Type Aircraft: Exploration Through High-Fidelity Aerodynamic Shape Optimization," Ph.D. thesis, University of Toronto, Toronto, ON, Nov. 2016.

[28] "A320/21," *ANA Cargo*, retrieved 11 March 2023. URL https://www.anacargo.jp/en/int/specification/a320.html.